Electronic Supplementary Information (ESI)

Optimizing Ionic Strength of Interfacial Electric Double Layer for Ultrahigh External Quantum Efficiency of Photomultiplication-Type Organic Photodetectors

Mingyun Kang,[a] Amit Kumar Harit,[b] Han Young Woo*[b] and Dae Sung Chung*[a]

[a.] Department of Chemical Engineering, Pohang University of Science and Technology (POSTECH), Pohang, 37673, Republic of Korea.

[b.] Department of Chemistry, KU-KIST Graduate School of Converging Science and Technology, Korea University, Seoul, 02841, Republic of Korea.

*Correspondence: hywoo@korea.ac.kr (H. Y. Woo)

*Correspondence: dchung@postech.ac.kr (D. S. Chung)

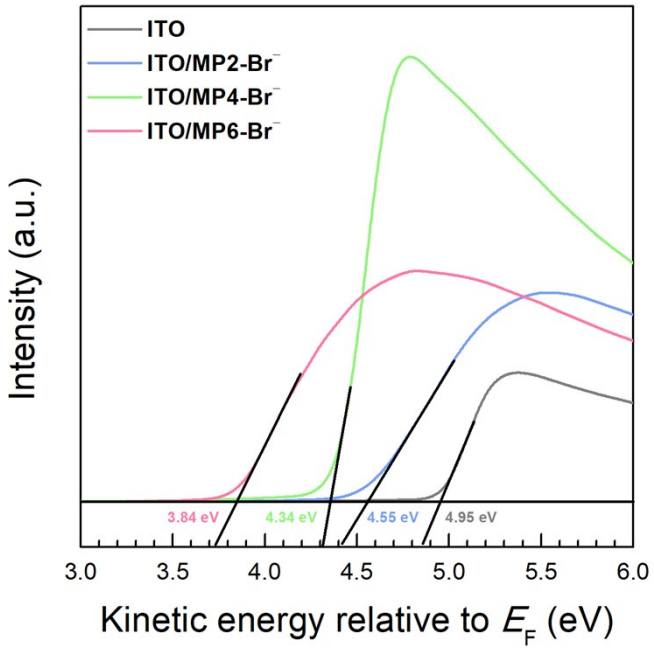

Fig. S1. Ultraviolet photoelectron spectroscopy (UPS) spectra of bare ITO and ITO/CPE surfaces in the secondary cutoff region.

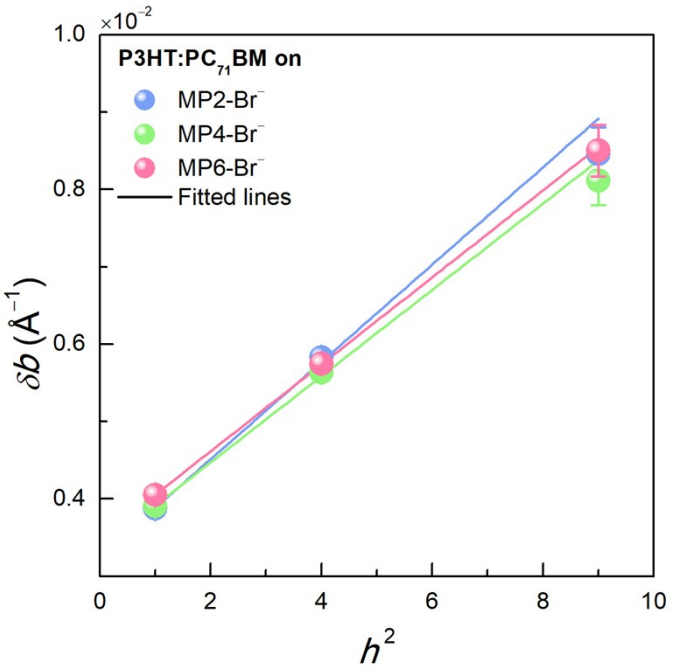

Fig. S2. δb–h^2 plots of P3HT:PC_{71}BM (100:1, w/w) films on PFP-based CPEs.

Drift–Diffusion Simulations

We employed the drift–diffusion approximation method, described in detail in previous studies, for the numerical simulations in the Fluxim software (Setfos), in order to model the transport, trapping, injection, and generation of the charge carriers.[1–5] Single-level trap states were assumed for simplicity, similar to various previous theoretical analyses of the charge transport.[6,7] In addition, the typical boundary conditions described by Schottky were applied in the simulation.[7,8] Under these conditions, the electron and hole densities at the semiconductor/electrode interfaces are assumed to remain constant under external biases and illumination. Because the electrons were spatially localized owing to the small amount of $PC_{71}BM$ dispersed in the P3HT matrix, the hole and electron mobilities of P3HT reported in a previous study were considered, that is, 10^{-4} and 5×10^{-8} cm^2 V^{-1} s^{-1}, respectively.[1,3] Based on the assumption that the Schottky junction between the ITO/CPE and P3HT can be transformed to a pseudo-Ohmic junction under illumination owing to band bending, different work function values were used for the dark and illuminated conditions;[9–12] these conditions were determined through temperature-dependent analyses. Optical parameters such as the refractive indices and extinction coefficients of the constituting layers were obtained from literature or measurements.[13] Details of the simulation parameters are presented in Table S1.

Table S1. Summary of parameters used in numerical simulations.

Temperature [K]	300
Thermionic work function of the cathode under dark condition [eV]	ITO/MP2–Br^-: 4.591 ITO/MP4–Br^-: 4.536 ITO/MP6–Br^-: 4.459

Thermionic work function of the cathode under illumination [eV]	ITO/MP2–Br^-: 4.888 ITO/MP4–Br^-: 4.905 ITO/MP6–Br^-: 4.952
Thermionic work function of the anode [eV]	5.00
HOMO level [eV]	5.20
LUMO level [eV]	3.20
N_0[a] [m^{-3}]	10^{29}
Dielectric constant	2.7
Charge carrier mobilities [$cm^2 V^{-1} s^{-1}$] **(based on SCLC analyses)**	μ_e: 5×10^{-8} μ_h: 1×10^{-4}
Trap density[b] [cm^{-3}]	10^{18}
Trap energy depth [eV]	MP2–Br^-: 0.621 MP4–Br^-: 0.650 MP6–Br^-: 0.709
Electron/hole capture rate[b] [$cm^3 s^{-1}$]	10^{-13}
Langevin recombination efficiency[c]	1
Non-radiative decay rate[c] [s^{-1}]	10^5
Generation efficiency[c]	1
Diffusion constant[c] [$cm^2 s^{-1}$]	0
Annihilation rate[c] [$cm^3 s^{-1}$]	0
Optical generation efficiency[c]	0.66
Pair separation[c] [nm]	1.285
Charge transfer type[c]	Onsager–Braun
Wavelength [nm]	550 (single wavelength)

Light intensity [W cm^{-2}]	3.80×10^{-6}

[a]Work function values of the cathodes were determined by temperature dependent analyses

[b]Parameters used in Reference 1

[c]Parameters used in References 3 and 13

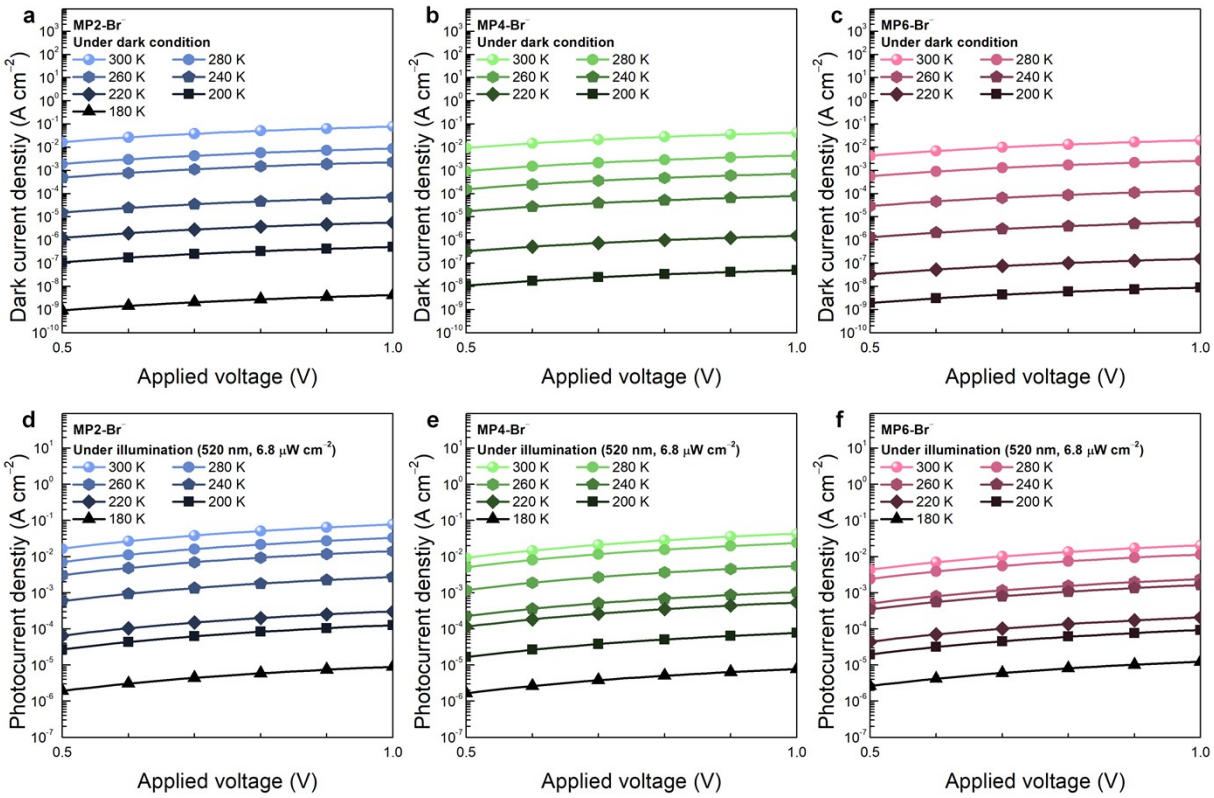

Fig. S3. a–c) Temperature-dependent dark *J*–*V* curves of optimized PM-OPDs based on (a) MP2–Br⁻, (b) MP4–Br⁻, and (c) MP6–Br⁻. d–f) Temperature-dependent illuminated *J*–*V* curves of the optimized PM-OPDs based on (d) MP2–Br⁻, (e) MP4–Br⁻, and (f) MP6–Br⁻.

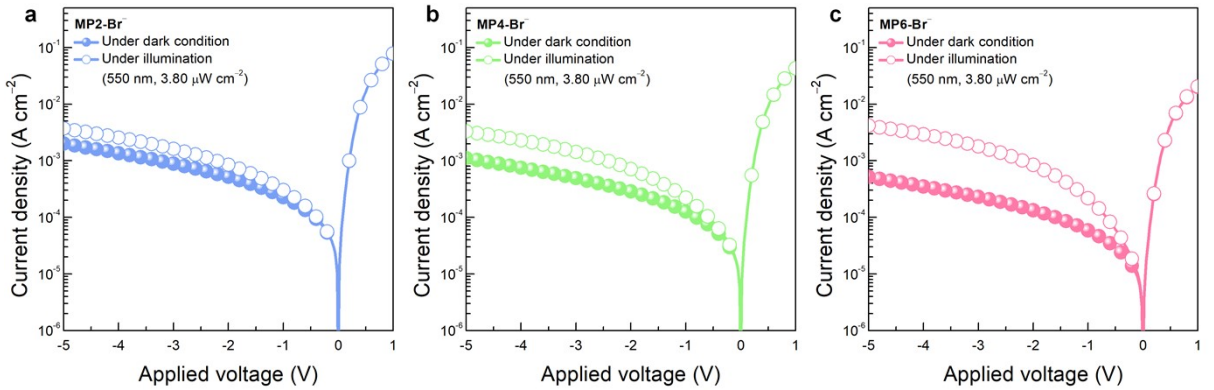

Fig. S4. a–c) Dark and illuminated *J*–*V* curves of optimized PM-OPDs based on (a) MP2–Br⁻, (b) MP4–Br⁻, and (c) MP6–Br⁻.

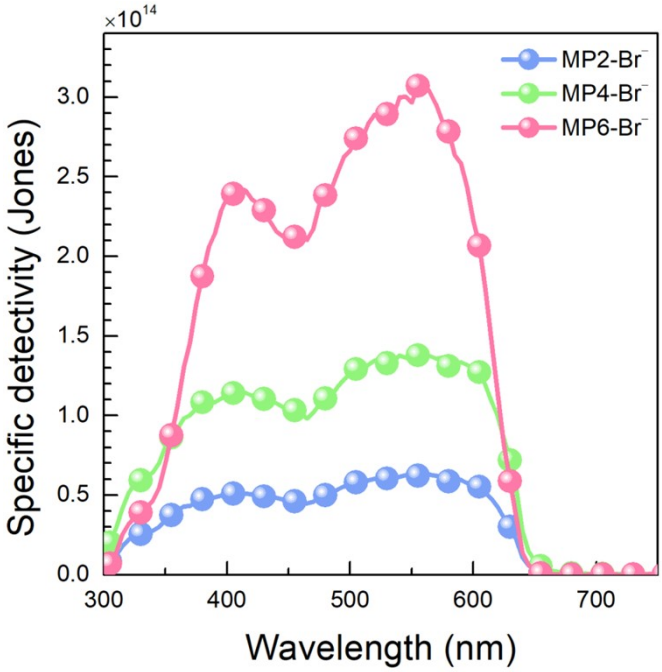

Fig. S5. Specific detectivity spectra of optimized PM-OPDs with PFP-based CPEs, as measured under a reverse bias of 15 V.

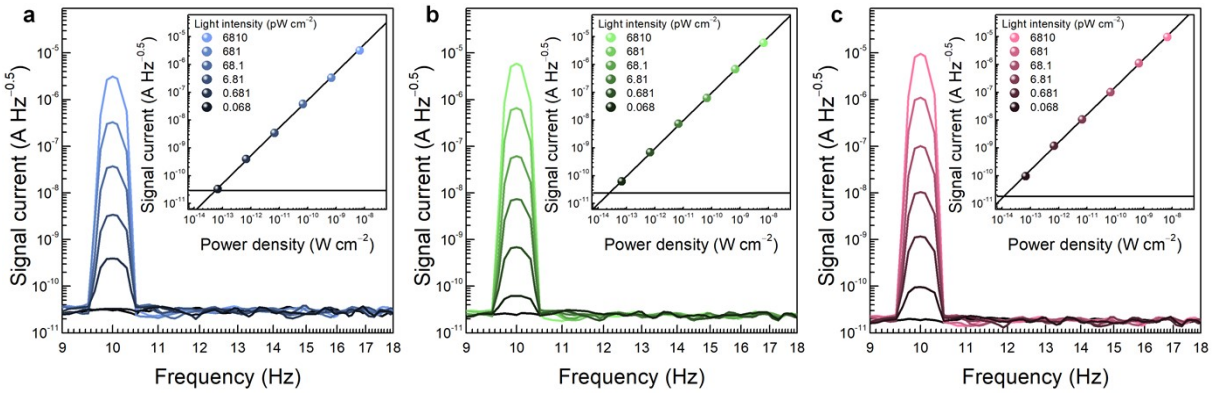

Fig. S6. a–c) Current spectral density plots of optimized PM-OPDs based on (a) MP2–Br^-, (b) MP4–Br^-, and (c) MP6–Br^-, under green light illumination (520 nm) with various light intensities and a modulation frequency of 10 Hz.

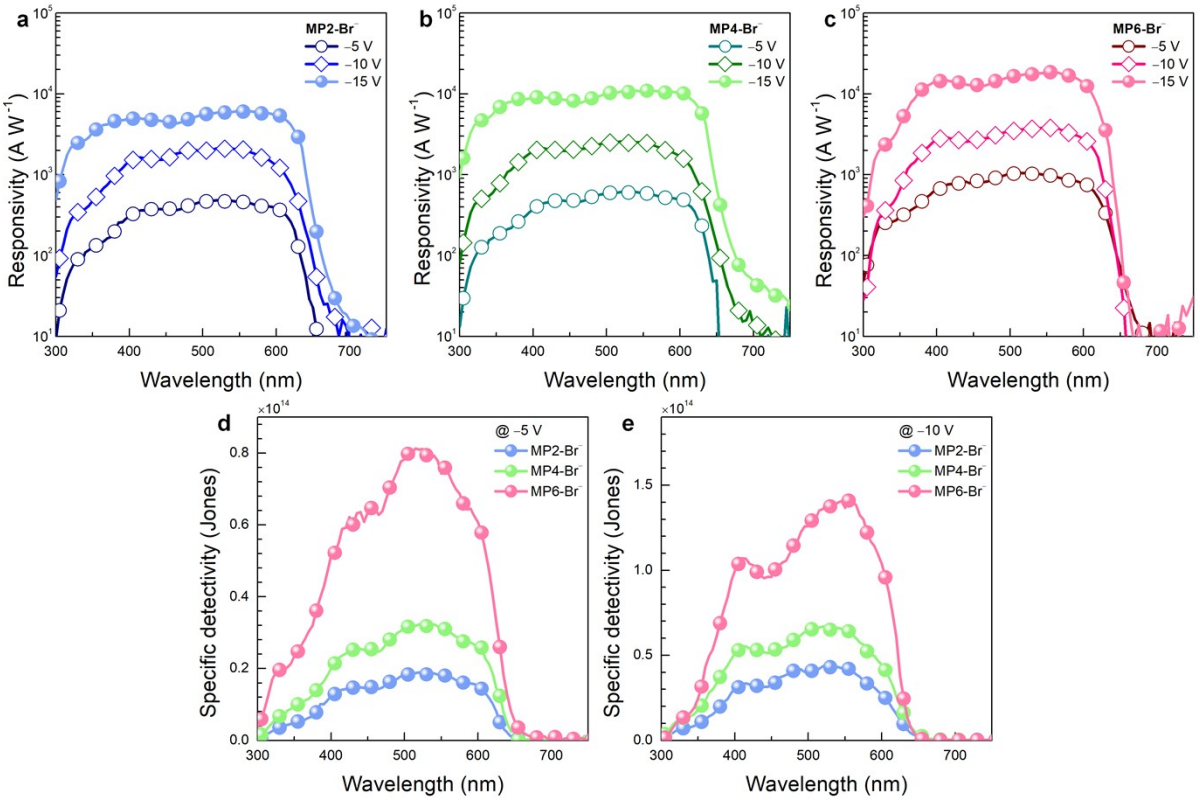

Fig. S7. a–c) Responsivity spectra of optimized PM-OPDs based on (a) MP2–Br^-, (b) MP4–Br^-, and (c) MP6–Br^-, measured under various reverse biases (−5, −10, and −15 V). d,e) Specific detectivity spectra of optimized PM-OPDs with the PFP-based CPEs, as measured at (d) −5 V and (e) −10 V.

Table S2. Summary of performances for optimized PM-OPDs with CPEs.

EDL	Applied Bias (V)	EQE_{max}(%)	R_{max} (A W^{-1})	D^*_{max} (Jones)
MP2–Br^-	−5	115,000	483	1.90×10^{13} [a]
	−10	516,000	2,120	4.36×10^{13} [a]
	−15	1,980,000	6,100	6.29×10^{13} [b]
MP4–Br^-	−5	147,000	615	3.26×10^{13} [a]
	−10	642,000	2,560	6.69×10^{13} [a]
	−15	2,760,000	11,000	1.39×10^{14} [b]
MP6–Br^-	−5	253,000	1,050	8.12×10^{13} [a]
	−10	881,000	3,800	1.41×10^{14} [a]
	−15	4,440,000	18,700	3.09×10^{14} [b]

[a]Specific detectivity values are calculated under the assumption that thermal noise is the only noise source ($D^* = \frac{R}{\sqrt{2qJ_d}}$)

[b]Specific detectivity values are obtained based on the NEP measurements

References

1. M. Daanoune, R. Clerc, B. Flament and L. Hirsch, *J. Appl. Phys.*, 2020, **127**, 055502.
2. S. Altazin, R. Clerc, R. Gwoziecki, G. Pananakakis, G. Ghibaudo and C. Serbutoviez, *Appl. Phys. Lett.*, 2011, **99**, 143301.
3. R. Häusermann, E. Knapp, M. Moos, N. A. Reinke, T. Flatz and B. Ruhstaller, *J. Appl. Phys.*, 2009, **106**, 104507.
4. L. J. A. Koster, E. C. P. Smits, V. D. Mihailetchi and P. W. M. Blom, *Phys. Rev. B*, 2005, **72**, 085205.
5. Fluxim AG, Information about SETFOS: Semiconducting Emissive Thin Film Optics Simulator Software; http://www.fluxim.com/setfos-intro (accessed: February 2022).
6. J. H. Jung and T. W. Kim, *J. Appl. Phys.*, 2011, **110**, 043721.
7. K. Marcin, M. Daanoune, O. Françoic-Martin, B. Flament, O. Dhez, A. K. Pankey, S. Chambon, R. Clerc and L. Hirsch, *Adv. Electron. Mater.*, 2018, **4**, 1700526.
8. D. A. Neamen, *Semiconductor physics and devices 3rd edition*, McGraw-Hill, New York, 2003.
9. M. Kang, S. Z. Hassan, S.-M. Ko, C. Choi, J. Kim, S. K. R. Parumala, Y.-H. Kim, Y. H. Jang, J. Yoon, D.-W. Jee and D. S. Chung, *Adv. Mater.*, 2022, **34**, 2200526.
10. J. Kim, M. Kang, S. Lee, C. So and D. S. Chung, *Adv. Mater.*, 2021, **33**, 2104689.
11. S. Yoon, G. S. Lee, K. M. Sim, M.-J. Kim, Y.-H. Kim and D. S. Chung, *Adv. Funct. Mater.*, 2021, **31**, 2006448.
12. D. K. Neethipathi, H. S. Ryu, M. S. Jang, S. Yoon, K. M. Sim, H. Y. Woo and D. S. Chung, *ACS Appl. Mater. Interfaces*, 2019, **11**, 21211–21217.
13. M. S. Jang, S. Yoon, K. M. Sim, J. Cho and D. S. Chung, *J. Phys. Chem. Lett.*, 2018, **9**, 8–12.
14. V. D. Mihailetchi, H. Xie, B. de Boer, J. A. Koster and P. W. M. Bom, *Adv. Funct. Mater.*, 2006, **16**, 699–708.